A 3D Shape Reconstruction of Ligament from Arthroscopic Images

Sakaguchi, Junpei
Department of Intelligent Machinery & Systems : Graduate Student

Katsuhara, Tadasuke
Department of Intelligent Machinery & Systems : Graduate Student

Hirokawa, Shunji
Department of Intelligent Machinery & Systems : Professor

出版情報：九州大学工学紀要. 66 (1), pp.15-28, 2006-03. 九州大学大学院工学研究院
バージョン：
権利関係：

Memoirs of the Faculty of Engineering, Kyushu University, Vol.66, No.1, March 2006

A 3D Shape Reconstruction of Ligament from Arthroscopic Images

by

Junpei SAKAGUCHI*, Tadasuke KATSUHARA* and Shunji HIROKAWA**

(Received January 25, 2006)

Abstract

In vivo data on the biomechanics of knee ligaments and their behavior under stress are necessary to understand and treat knee injuries. To obtain this data, accurate measurement of strains on and in the ligament is necessary. Technical and ethical considerations make such *in vivo* measurements of a human knee difficult or impossible. To overcome these problems, we planned to combine two techniques to measure stress/strain distributions; One is an arthroscopic measurement of ligament's deformation. The other is to introduce stress/strain distributions using the deformation data through the FEM analysis. The objective of this study was to establish the method to obtain the 3D deformations from the arthroscopic images. The endoscopic photos were converted into grey scale images, and the shape from shading method was used to generate the objects' 3D shape from the images. Once the system was calibrated, a swine femur and tibia were set in a special fixture, and the industrial endoscope was used to pictures of the anterior cruciate ligament (ACL) at various angles of knee flexion. Three-dimensional coordinates were obtained by the level set method from the brightness data on the processed image and the three-dimensional shape of the ACL surface was generated.

Keywords: *In vivo* measurement, Arthroscopy, Anterior cruciate ligament, Shape from shading

1. Introduction

Quantitative *in vivo* data on the biomechanics of knee ligaments and their behavior under stress are essential for understanding knee ligament injuries, for successful repair or reconstruction of ligaments, and for the design of prosthetic ligaments. To study the detailed mechanics of the ligaments, especially of the anterior cruciate ligament (ACL), accurate measurement of strains on and in the ligament is necessary.

Although there are numerous *in-vitro* studies of strains on the ligament caused by knee motion, there are virtually no *in vivo* studies because the invasive procedures needed to conduct them can

* Graduate Student, Department of Intelligent Machinery & Systems
** Professor, Department of Intelligent Machinery & Systems

damage the ligaments.

Beynnon et al. [1] attempted one such study by suturing electric strain sensors to the ligament in a living subject's knee. Beynnon et al.'s experiment has been performed in some other countries. This invasive operation is highly controversial, and there is debate about whether the data thus obtained are worth the risk to the patient. It should be noted that the above-mentioned *in vivo* study provided results closer to actual clinical cases than those obtained from *in-vitro* studies, thereby demonstrating how important the *in vivo* experiments are. In Japan, the law does not permit experiments of this sort to be done. A method which allows accurate *in vivo* measurement but which is not as invasive as Beynnon, et. al's is needed.

In this study, we have used a combination of arthroscopy and image analysis to study *in vivo* strain on a swine ligament. In an earlier study, we applied Tan and Ishikawa's proposed modified motion capture system [2] which uses arthroscopic examination to detect the 3D positions of markers or speckles, on the ACL's surface. When we used the technique to measure strain on a swine ACL or a human ACL *in vitro*, we found the markers did not scatter enough for effective measurement of surface strain. As an alternative, we reconstructed the ACL's shapes and deformations in three dimensions by applying the "shape from shading method" [3), 4)] in which the 3D shape of an object is reconstructed by measuring variations in brightness on the surface. Okatani and Deguchi [4] applied the method to endoscopic images of a human stomach's inner wall to reconstruct its shape. In the present study, we used an industrial endoscope to record images of a swine ACL at various knee angles. Using the shape from shading method, we reconstructed the ACL's 3D shapes at various angles of flexion.

Once we obtain the 3D shapes and deformations of the ACL at various knee angles, then we will be able to use the shape and deformation data for curvature analysis or FEM analysis [5] to study strain distribution on the ligament. This idea came from our experience that we could easily determine which portions of the ACL are tense through the arthroscopic examination qualitatively but unfortunately not quantitatively.

2. A 3D Shape Reconstruction from Brightness Variation

2.1 Brightness on a surface point

A *Lambertian* surface exhibits perfect diffuse reflection. In the case of a Lambertian surface, brightness is in direct proportion to the intensity of light which comes onto the surface.

Figure 1 illustrates the reflection geometry of an optical system. If only a single incident ray from a light source strikes a surface patch, then brightness E_i at *P* is expressed as,

$$E_i = I_0 \frac{\cos\theta_i}{r^2} \tag{1}$$

where I_0 is the intensity of the light source, θ_i is the angle of incidence and *r* is the distance between point *P* and the light source.

Let the reflected light's component of intensity at *P* toward the camera be L, then L is expressed as functions of angle θ_i, θ_r and ϕ_r shown in **Fig.1**,

$$L = F(\theta_i, \theta_r, \phi_r) E_i \tag{2}$$

where, θ_i, θ_r and ϕ_r are the incident angle, the reflection angle and the azimuth angle

respectively, and $F(\theta_i,\theta_r,\phi_r)$ called as the *Bidirectional Reflectance Distribution Function(BRDF)* [6] is a measure of the reflection characteristic and is dependent on the material and surface roughness of the object.

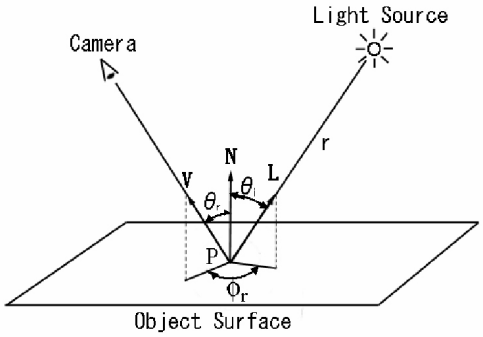

Fig.1 Local coordinates on a surface patch for describing the light source and camera positions.

From Eq. (1) and (2), the relation

$$L = I_0 \frac{F(\theta_i,\theta_r,\phi_r)\cos\theta_i}{r^2} \tag{3}$$

holds. Then, the component toward the camera's direction of E_i is expressed by the following image irradiance equation.

$$E_r = \sigma \frac{F(\theta_i,\theta_r,\phi_r)\cos\theta_i}{r^2} \tag{4}$$

where σ is a constant depending on both the camera parameters and I_0.

2.2 An endoscope's optical system

In an endoscope, the center of the lens and the light source are located in the same position as shown in **Fig.2**. Thus, setting $\theta_i = \theta_r = \theta$ in **Fig.1**, the BRDF in Eq.(4) can be simply expressed as $F(\theta,\theta,0)$. If a surface is Lambertian, $F(\theta,\theta,0)$ is known to degrade to a monotonous function of θ and therefore $F(\theta,\theta,0)\cos\theta$ can be simply expressed as $F(\cos\theta)$. Further denoting $E_r = E$, Eq.(4) can be expressed by a simpler form as,

$$E = \sigma \frac{F(\cos\theta)}{r^2} \tag{5}$$

From Eq.(5), we may conclude that for an endoscope, brightness E at P can be expressed as functions of surface gradient θ and the distance from the light r.

For the optical geometry of the lens as shown in **Fig.2**, the Cartesian coordinate is set so that the projection center is located at the origin, the x-y plane is parallel to the image plane, and the z-axis is perpendicular to the image plane. The focal distance of the camera lens is expressed by *f*, and an ideal point light source is assumed to be located at the origin.

Formally, $E_r(=E)$ and L appeared in Eq.(2) are called as illumination intensity (Energy per unit area) and luminance intensity (Energy per unit area and per unit vertical angle) respectively.

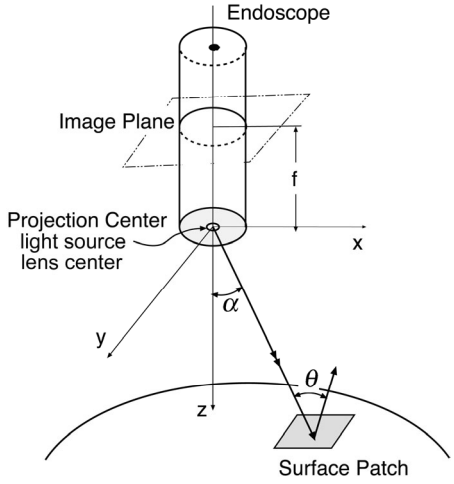

Fig.2 The optical system of the endoscope.

For a Lambertian surface, the illumination intensity is in direct proportion to the luminance intensity. The relationship between E and L for the optical geometry of the lens can be expressed by [7],

$$E = L\frac{\pi}{4}\left(\frac{d}{f}\right)^2 \cos^4\alpha \tag{6}$$

where d is the lens diameter, and α (illumination angle) is the angle between the optical axis and the line connecting the light source and a surface point P.

Equation (6) shows that illumination intensity decreases as a function of α. In actual optical equipment, several lenses are installed to compensate for this decrease. Still, a linear relationship between E and L holds same as a single lens is used.

2.3 3D shape reconstruction[3]

From Eq.(5), we know that brightness E can be determined by the values of surface gradient θ, and the light source distance r. However, neither θ or r can be introduced from E, because both the variables are interrelated. If r in Eq.(5) is constant, the surface gradient θ can be introduced from brightness E. Thus, we first draw on the object's surface an imaginary line on which every point is equally distant from the light source. This line is called *an equal-distance contour*. As shown in **Fig.3**, an equal distance contour is the intersection between the object surface and a spherical shell with radius r whose center is at the light source.

At a point on a surface, a tangent vector $\boldsymbol{T}$ and a normal vector $\boldsymbol{N}$ are known to be orthogonal with each other. While at a point on an equal distance contour, the tangent vector $\widetilde{\boldsymbol{T}}$ of that equal distance contour and a normal vector $\boldsymbol{N}$ are orthogonal to each other, and therefore the degree of $\boldsymbol{N}$'s freedom is reduced from 2 to 1. Thus from Eq.(5), we may reconstruct an object shape at part of a narrow strip along an equal distance contour.

The entire shape of an object can be reconstructed by solving an evolution equation with respect to an equal distance contour. Solving an evolution equation is to derive a new equal distance contour using the data of the present contour whose distances are $r+\Delta r$ and r from the light source respectively.

An initial loop around a singular point is required as a source for propagating equal distance

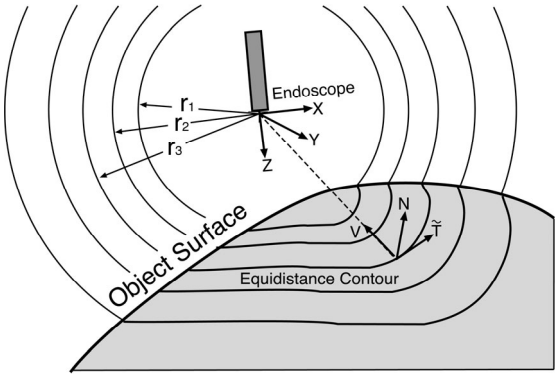

Fig.3 The propagation of equal-distance contours.

contours. If the initial loop is small enough, its shape has little effect on the successive formation of the equal distance contours. Thus a small circle can be chosen as the initial loop. When the object's shape is convex, the brightest point over the surface may be chosen as the singular point, because the brightest point usually corresponds to the point nearest the light source and the norm for the surface at that point directs toward the light source (see P_0 in **Fig.3**). Starting from a small circle around the brightest point, one may extend the solution for the evolution equation with respect to an equal distance contour.

2.4 Propagating an equal distance contour

Given a projection of an equal distance contour onto the image plane, propagation of the equal distance contour is mathematically determined by an expanding rate of the projection contour.

Suppose an point $\boldsymbol{x} = (x, y)$ on the projection contour moves to $\boldsymbol{x}' = \boldsymbol{x} + \delta d\boldsymbol{n}$ according as a point $\boldsymbol{X}$ on the equal distance contour moves to $\boldsymbol{X}'$ as shown in **Fig.4**.

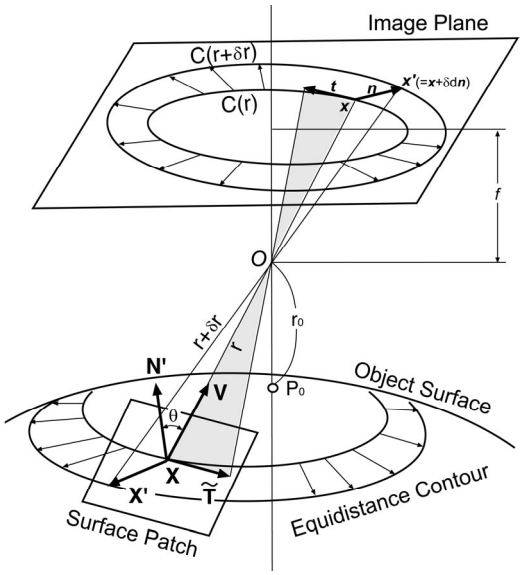

Fig.4 The evolution of an equal-distance contour.

Where $\boldsymbol{n} = (n_x, n_y)$ is a unit vector normal to the projection contour at point $\boldsymbol{x}$ and δd is the distance between $\boldsymbol{x}$ and $\boldsymbol{x}'$ in the direction of $\boldsymbol{n}$.

From perspective transformation, the relationships between $\boldsymbol{X}$ and $\boldsymbol{x}$, and $\boldsymbol{X}'$ and $\boldsymbol{x}'$ are represented respectively as

$$\boldsymbol{X} = \frac{\boldsymbol{x}}{|\boldsymbol{x}|} r \tag{7}$$

$$\boldsymbol{X}' = \frac{\boldsymbol{x}'}{|\boldsymbol{x}'|} (r + \delta r) \tag{8}$$

If $\boldsymbol{X}$ is small enough, then we may assume that $\boldsymbol{X}'$ is on the tangential plane. Then, the following relation,

$$\boldsymbol{N}(\boldsymbol{X}' - \boldsymbol{X}) = 0 \tag{9}$$

holds, where $\boldsymbol{N}$ is the unit normal vector of the tangential plane. Since the tangential vector $\widetilde{\boldsymbol{T}}$ of the equal distance contour is on the tangential plane, the following relation,

$$\boldsymbol{N}\widetilde{\boldsymbol{T}} = 0 \tag{10}$$

holds as well.

In **Fig.4**, $\boldsymbol{t} = (n_x, -n_y)$ is a unit tangential vector of the projection contour at $\boldsymbol{x}$, and $\boldsymbol{V}$ is a unit vector from $\boldsymbol{X}$ to O ($\boldsymbol{NV} = \cos\theta$). From **Fig.4**, we know that $\widetilde{\boldsymbol{T}}$ can be represented with a linear relation with the vectors $\boldsymbol{t}$ and $\boldsymbol{V}$, because it is on the plane made by these two vectors.

Thus from Eq.(7) through (10) and the abovementioned relations, we may introduce the following equation,

$$\frac{\delta d}{\delta r} = \frac{\sqrt{(x^2 + y^2 + f^2)\{f^2(n_x^2 + n_y^2) + (xn_x + yn_y)^2\}}}{fr(n_x^2 + n_y^2)} \cdot \frac{1}{\tan\theta} \tag{11}$$

where f is the focal distance of a lens.

Equation (11) describes a deforming fashion of the projection curve as a function of *r*. Here we may rewrite Eq.(5) as,

$$\cos\theta = F^{-1}(r^2 E(x, y)/\sigma) \tag{12}$$

where brightness E was expressed as functions of x and y as $E(x, y)$. From Eq.(12), the relation

$$\tan\theta = \frac{\sqrt{1 - \{F^{-1}(r^2 E(x, y)/\sigma)\}^2}}{F^{-1}(r^2 E(x, y)/\sigma)} \tag{13}$$

is introduced. Substituting Eq.(13) into Eq.(11), we obtain the following relation,

$$\frac{\delta d}{\delta r} = \frac{F^{-1}(r^2 E(x,y)/\sigma)\sqrt{(x^2+y^2+f^2)\{f^2(n_1^2+n_2^2)+(xn_1+yn_2)^2\}}}{fr(n_1^2+n_2^2)\sqrt{1-[F^{-1}(r^2 E(x,y)/\sigma)]^2}} \tag{14}$$

This completes the formulation of propagation for an equal distance contour. In order to solve Eq. (14), we will have to apply *the level set method* which has been developed in the material science field. Numerical solutions on the level set method have been detailed in the literature [4), 8), 9)], which will be omitted here.

3. Experiments and Results

3.1 Determination of optical parameters for the endoscope system

We first set up and calibrated the endoscopic system by using it to photograph a series of test objects. We used an industrial endoscope (VH-B61, Keyence Co., Japan) together with an image recording device (VH-5000, Keyence Co., Japan). We chose this endoscope because the aberration it produces is lower than that of clinical endoscopes. The endoscope's specifications are described in **Table 1**.

Table1 The specifications of the endoscope.

Diameter of long cylinder	6 mm
Direction of field of view	0° (direct viewing)
Effective length	300 mm
Angle of field	55°
Depth of observation	2~50 mm
Range of view	ϕ2~ϕ55 mm
Pixel size in the output apparatus	0.23 mm/pixel

Photographic parameters such as the angle of view and the focal distance of the lens are known to vary depending upon the refractive index of the media. In a clinic, the joint cavity is filled with a saline solution during arthroscopic examination [10)]. To make our experimental conditions match clinical ones, we immersed the test objects and the endoscope lens in a saline solution. Consequently all our endoscope system's parameter values (aberration correction, shading correction, the projection center coordinates [11)]) were obtained this way. These values were used in the shape from shading calculations. The focal distance of our endoscope system was 36 mm in air, and 48 mm in the saline solution. It should be noted that saline solution caused much less localized mirror reflection or mutual reflection much than air does.

The measure of brightness was determined by gray scale. The brightness of each image pixel was classified in one of the 256 gray scale pixels. The relationship between brightness $\varepsilon(in\,256\,level)$ and surface gradient θ was determined as,

$$\varepsilon = \varepsilon_{\max}\cos\theta \tag{15}$$

where $\varepsilon_{\max}$ indicates the brightest value. At the brightest point, the relation $\cos\theta = 1$ usually holds.

Next, the relationship between brightness and light source distance was ascertained. The light source distance was measured by a range finder. The gray-level threshold was applied to specify the brightest point. Variations in the brightest value $\varepsilon_{\max}$ plotted against the light source distance

$r\,(mm)$ were introduced as shown in **Fig.5**. From **Fig.5**, we used the following relation in the measurement experiments.

$$\begin{cases} \varepsilon_{\max} = 255 & r < 12 \\ \varepsilon_{\max} = 5137 r^{-1.16} & r \geq 12 \end{cases} \tag{16}$$

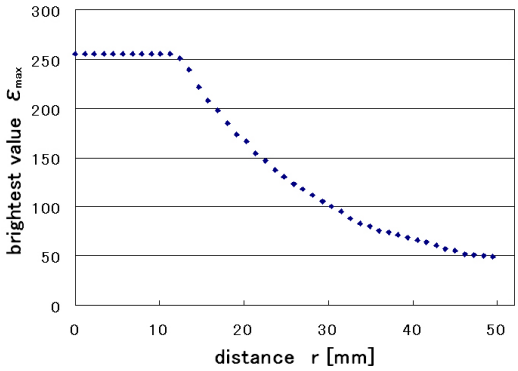

Fig.5 Variations in the brightest values plotted against the light source distances.

We next determined whether the relation in Eq.(6) held for an optical system immersed in a saline solution. We calculated the theoretical relationship between brightness ε_{th} and the cosine of the illumination angle α. We used a computer-generated square of uniform gray color with a known reflection value and the relation was introduced as almost rectilinear as shown in **Fig.6**. We then set our optical system to duplicate the above theoretical geometry. Brightness ε at a point on a real dark gray linoleum plate was measured and recorded together with the coordinate of that point. The values of ε were plotted against $\cos\alpha$ on the same graph (**Fig.6**). After that, using the least square method, we introduced the power of $\cos\alpha$ so that the measured points fit best to the theoretical line. According to Eq.(6), ε_{th} should be in proportion to $\cos^4\alpha$; however, we found $\cos^{3.84}\alpha_{th}$ was best for an optical system immersed in a saline solution. The data after the correction by the value of $\cos^{3.84}\alpha$ are also plotted in **Fig. 6**.

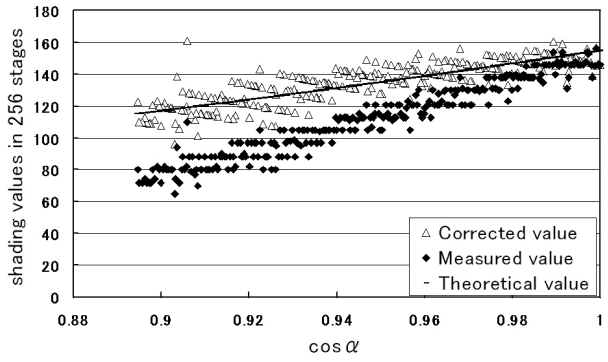

Fig.6 The theoretical, the measured and their corrected values of brightness plotted against the cosine of the illumination angle.

3.2 Examination of reconstruction accuracy

We checked the accuracy of the proposed algorithm by applying it to several clay objects with Lambertian surfaces. They were a sphere 20 mm in diameter; a cylinder 40 mm long and 20 mm in diameter, and an object of ligament-like shape approximately 40 mm long, 10 mm wide and 3 mm thick. The ligament-like object was made so as to mimic the shape of an actual anterior cruciate ligament (ACL) of a swine hind limb at 60°of knee angle. First, each object was scanned by a 3D laser scanner (TDS-530; Pulstec Co., Ltd., Japan), whose measurement error was less than 0.03 mm. and the resulting 3D images were saved. Next, each object and the arthroscope lens were immersed in saline solution and one photo of each object was taken through the arthroscope lens.

The photos were scanned into a computer and the shape of each object was reconstructed through the proposed algorithm. The images obtained by scanner and by reconstruction were then compared. For each object, the difference between the scanned image and the reconstructed image in the z-direction was calculated with respect to each measured datum. The root mean square (RMS) value for the above mentioned distances for all the data was then calculated to assess the accuracy of the reconstructed surface. The RMS values for the generated and real object surfaces fell in a range between 0.51 and 0.94 mm. We then introduced the relative RMS values, i.e. the values of RMS divided by the object size. The RMS value for each of generated and real object surfaces was divided by its diameter for the sphere and by a diagonal line the length of its base for the cylinder and the ligament like object in shape respectively. The values were from 1.6 to 2.7 %.

3.3 Photographing of a swine ACL and its shape reconstruction

3.3.1 Materials and methods for photographing

Figure 7 shows the experimental setup before it was put into a tub filled with saline solution. An intact ACL from a swine hind limb was used. To reproduce natural knee motion, we used a special apparatus, designated a knee motion simulator jig, which had been used in experiments with human cadaver knees [12].

The swine limb was fixed in the simulator jig. The proximal end of the femur and the distal end of the tibia were firmly secured in the holders. Unlike the flexible scope used in clinics, the industrial endoscope is a long, rigid pipe, and its angle of insertion cannot be changed easily, so we were unable to get good views of the ACL at any insertion positions and/or angles. We decided to remove the patella and take images of the ACL's frontal view. The endoscope head was set at 70° to the femoral axis. Since the intact ACL had red patches on the surface because of bleeding, the reflection index was not uniform over the surface. We covered the endoscope head with red cellophane. By illuminating the ACL's surface with red light, we made the reflection index uniform.

The holder with the tibia was moved so that the joint flexed from 15 to 100° in increments of 5°. At each increment, the image of the ACL was taken through the endoscope. In all, 18 images were recorded and stored in a computer. To eliminate possible influences of diffused reflection of light for determining the brightest point and the brightest value, we applied a median filtering process on the image.

3.3.2 Reconstruction of the ACL shape

We first converted the colored bit-map images to gray-scale images, and scaled each image to 170 × 170 pixels. **Figure 8 (a)** through **(e)** show the gray-scale images of the ACL at various knee angles. In each figure, the ACL is seen in the center and the femoral condyles on the upper part. We

extracted the image of the ACL by manually blackening the surrounding area as shown in **Fig.9**. By

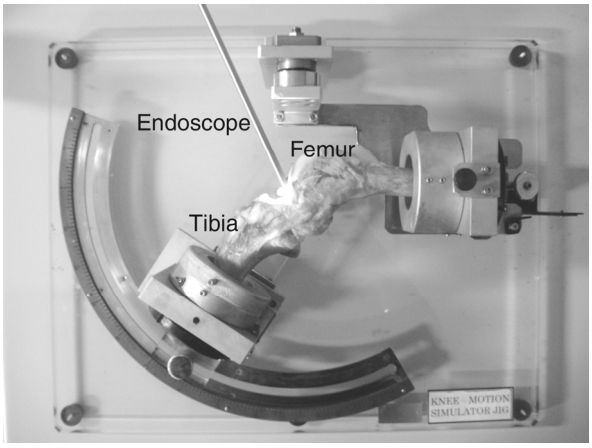

Fig.7 Experimental set up.

applying the shape from shading algorithm to each image in **Fig.8**, we drew equal distance contour maps as shown in **Fig.10**. Finally, we converted the 3D data along equal distance contours into 3D point data in the Cartesian coordinates. **Figure 11** shows scatter diagrams of the 3D point data of the ACL surface. In the figure, points are shaded in proportion to their height in the z-direction. This completed the shape from shading process for the ACL.

We described the ACL surface by applying the B-spline equation to the 3D data. Once the object shape was described mathematically, it was possible to represent the shape as viewed from any direction. **Figure 12** shows the shading models of the ACL at 60° of knee flexion as viewed from rotation around the tibial axis at 45° of intervals. It should be stressed that these eight images were made only from brightness distribution of a single image.

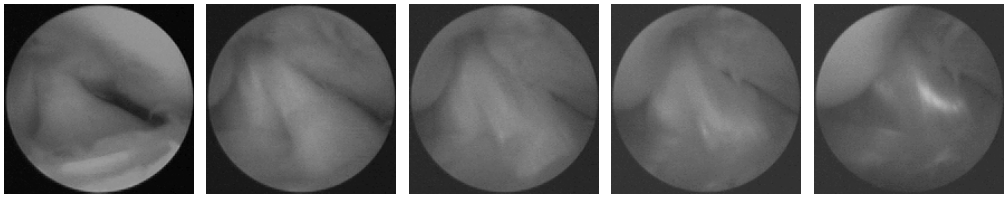

(a)knee angle:20° (b)40° (c)60° (d)80° (e)100°

Fig.8 Arthroscopic images of the swine ACL at various knee angles.

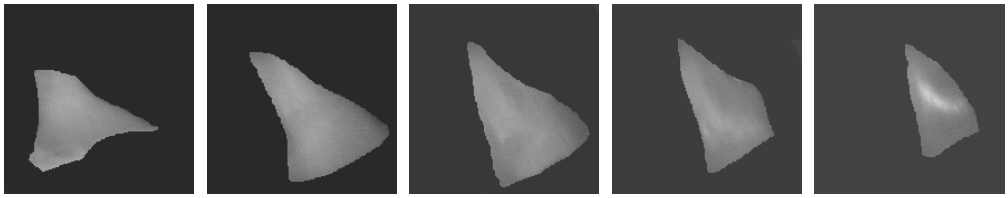

(a)knee angle:20° (b)40° (c)60° (d)80° (e)100°

Fig.9 Images of the ACL obtained by blackening the surrounding area.

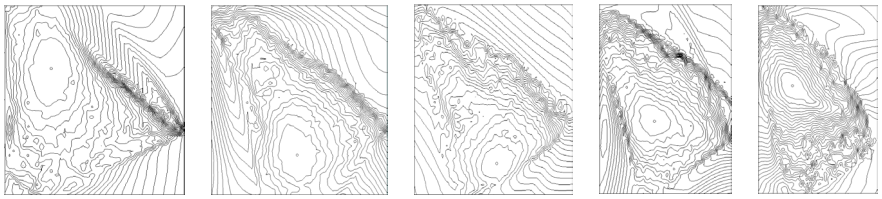

a)knee angle:20° (b)40° (c)60° (d)80° (e)100°

Fig.10 Equal-distance contour maps of the ACL at various knee angles.

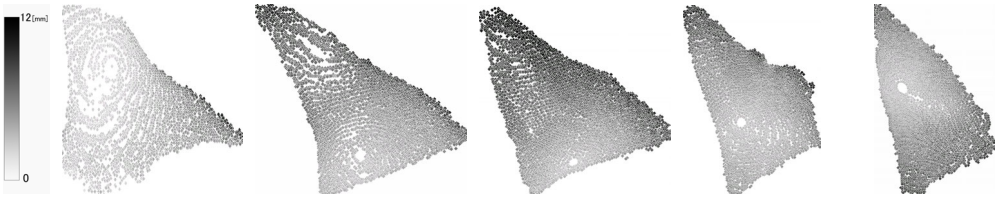

(a)knee angle: 20° (b)40° (c)60° (d)80° (e)100°

Fig.11 Scatter diagrams of the ACL's surface points shaded in proportion to their height values.

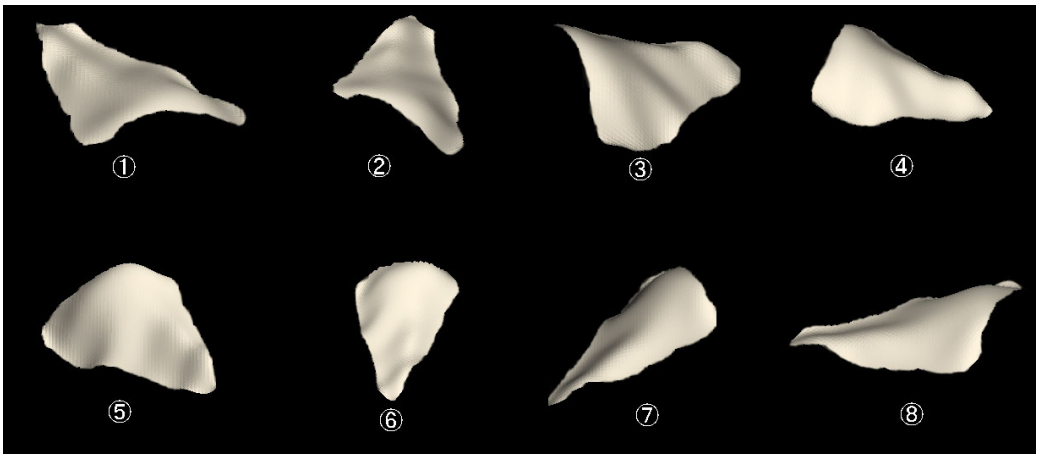

Fig.12 Shading models of the ACL viewed from various directions (at knee flexion angle of 60°).

4. Discussion

4.1 Shape reconstruction accuracy

Initially, we thought that measuring strain distribution by applying the shape from shading method to the ACL surface would be impractical: the method's reconstruction accuracy is poor compared to direct methods such that used by Beynnon, et. al.[1]. Contrary to expectations, reconstruction error was less than 3%. Because ligaments experience large and highly variable strains in association with knee motion, our method, with necessary modifications, might be more useful than other methods for measuring ligament deformation, and may permit non-invasive or less- invasive in-vivo measurement.

There has been a suspicion that the shape from shading algorithm is limited in its application; it has been thought that the object's surface roughness and the luminance intensity must be uniform

over the entire surface. Nevertheless, only a Lambertian surface is required for the algorithm to work reasonably well, and most biological soft tissues satisfy the requirement. Furthermore, photographing in a saline solution suppressed the localized mirror reflections or mutual reflections which can happen in air. Reconstruction accuracy can be further improved by mathematically synthesizing more than two shapes reconstructed from ligament images viewed in the same position but from different directions

To improve measurement accuracies, two problems must be solved. The first problem is how to determine exactly where the ligament ends and bone begins. Even by eye, it was sometimes difficult to distinguish the ligament from the bone at the insertions. An application of the edge detection technique available for image processing might solve this problem. The second is how to measure the exact distance between the brightest point on the surface and the light source. In the preliminary examination, we assumed the relationship between the brightness values at the surface point and its distance from the light source was that shown in **Fig.4** and Eq.(8). We used this relationship to model the ACL shape. Yet the brightness value and light source distance are not identical. A focus function with higher precision should be installed in the endoscope to measure the exact distance.

4.2 Methods for introducing ligament's strain from the shape

Once we obtain the 3D shapes/deformations of the ligament at various knee angles, strain distributions on the ligament can be introduced in several ways. One of the simplest ways may be, by representing the fiber bundles with geodesic lines, to introduce strain values along them.

Figure 13 illustrates the way. In **Fig.13**, points $f_1,t_1,..f'_1,t'_1,..$are marked out in equal increments along the femoral and the tibial insertion lines (10 increments in **Fig.13**).

Surface equations S and S' can be introduced through our arthroscopic measurement. Then *geodesic lines* at different knee angles $f_i t_i$ and $f_i' t_i'$ respectively are introduced and thus strain along that line can be introduced as,

$$\delta_i = \frac{f_i' t_i' - f_i t_i}{f_i t_i} \tag{17}$$

A more feasible way to introduce stress and strain distribution over the ligament's surface is to apply shape/deformation data to a fiber-reinforced hyper-elastic model [5].

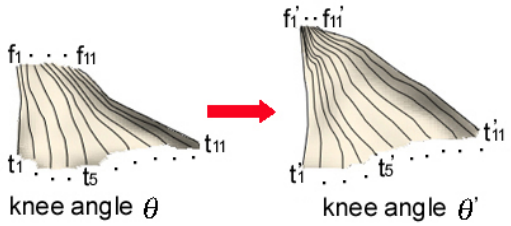

Fig.13 Geodesic lines on the ligaments at different knee angles.

4.3 Clinical application

To use this method on human subjects, a special endoscope is needed. Because clinical endoscopes are equipped with flexible fiber optic cables and fish-eye lenses or cross-eye lenses, using one in a study like this would require not only a complex calculation for the luminance and illuminating intensities but also a complex correction of the optical path's geometry [13]. For this reason, we used an industrial endoscope. However, because the industrial model had a rigid fiber

optic conduit, to obtain the necessary viewing angle(s), we had to remove the entire patella, which cannot be done in a human in-vivo study. Either an endoscope with the flexible probe of a clinical model and the low optical aberration of an industrial model or software to perform the necessary complex calculations described above is necessary.

5. Conclusion

We have developed a system to reconstruct a ligament's shape through arthroscopic measurement. We took images of a swine ACL at various knee angles through an industrial endoscope and reconstructed the 3D shape of the ACL. Examination of reconstruction accuracy by applying the algorithm to several synthetic and real object images demonstrated that the relative error was less than 3%. The system has the potential to allow accurate in vivo measurement of strain on the ligament without severely invasive surgical procedures. To use this method for studying the human ACL, either an endoscope with the flexible probe of a clinical model and the low optical aberration of an industrial model or software to perform the necessary complex calculations described above is necessary.

Acknowledgements

The authors thank Professor Koichiro Deguchi and Associate Professor Takayuki Okatani, Graduate School of Information Sciences, Tohoku University, Japan, for their help of this project. They also thank to Mr. Steven Sabotta for reading this manuscript.

References

1) B. Beynnon, J.G. Howe, et al., The Measurement of Anterior Cruciate Ligament Strain In-Vivo, *International Orthopaedics*, vol.16, pp.1-22, 1992.
2) J.K. Tan and S. Ishikawa, Human Motion Recovery by the Factorization Based on a Spatio-Temporal Measurement Matrix, *Computer Vision and Image Understanding*, vol.82, no.2, pp.101-109, 2001.
3) R. Kimmel and A.M. Brucksten, Tracking Level Sets by Level Sets: A Method for Solving the Shape from Shading Problem, *Computer Vision and Image Understanding*, vol.62, no.2, pp.47-58, 1995.
4) T. Okatani and K. Deguchi, Shape Reconstruction from an Endoscope Image by Shape from Shading Technique for a Point Light Source at the Projection Center, *Computer Vision and Image Understanding*, vol.66, no.2, pp.119-131, 1997.
5) S. Hirokawa and R. Tsuruno, Three-dimensional Deformation and Stress Distribution in an Analytical/Computational Model of the Anterior Cruciate Ligament, *Journal of Biomechanics*, vol.33, no.9, pp.1069-1077, 2000.
6) B.K.P. Horn and R.W. Sjoberg, Calculating the reflectance map, *Applied Optics*, vol.18, no.11, pp.1770-1779, 1979.
7) B.K.P. Horn, *Robot Vision*, MIT Press and McGraw Hill, 1986.
8) S. Osher and J.A. Sethian, Fronts propagating Hamilton-Jacobi formulations, *J. Comput. Phys.*, vol.70, pp.12-49, 1988.
9) J.A. Sethian and J. Strain, Crystal growth and dendritic solidification, *J. Comput. Phys.*, vol.98, pp.231-253, 1992.

10) R. Viola, N. Marzano and R. Vianello, An Unusual Epidemic of StaphyLococcus-NegativeInfections Involving Anterior Cruciate Ligament Reconstruction with Salvage of the Graft Function, *J. Arthroscopic and Related Surgery*, vol.16, no.2, pp.173-177, 2000.
11) H. Haheishi, Y. Yagihashi and Y. Miyake, A New Method for Distortion Correction of Electronic Endoscope Images, *IEEE Trans. Med. Imag.*, vol.14, no.3, pp.548-555, 1995.
12) S. Hirokawa, K. Yamamoto and T. Kawada, Circumferential Measurement and Analysis of Strain Distribution in the Human ACL using a Photoelastic Coating Method, *Journal of Biomechanics*, vol.34, no.9, pp.1135-1143, 2001.
13) S. Shah and J.K. Aggarwal, Intrinsic Parameter Calibration Procedure for A (High-Distortion) Fish-Eye Lens Camera with Distortion Model and Accuracy Estimation, *Pattern Recognition*, vol.29, no.11, 1775-1788, 1996.